RSC Advances

RSC Publishing

PAPER

View Article Online
View Journal | View Issue

# Role of $TiO_2$ morphological characteristics in EVOH–$TiO_2$ nanocomposite films: self-degradation and self-cleaning properties

Cite this: *RSC Advances*, 2013, **3**, 8541

Konstantinos C. Christoforidis,[a] Anna Kubacka,[a] Manuel Ferrer,[a] María L. Cerrada,[b] Marta Fernández-García*[b] and Marcos Fernández-García*[a]

Received 11th December 2012,
Accepted 25th March 2013

DOI: 10.1039/c3ra23271a

**www.rsc.org/advances**

The role of $TiO_2$ morphological characteristics in the ultimate performance of advanced, light-triggered EVOH–$TiO_2$ nanocomposite films is analyzed using four different inorganic anatase-$TiO_2$ materials obtained from the same initial solid precursor. Morphological variations in the inorganic component lead to differences in the inorganic–organic interface, described here through a detailed structural investigation using wide angle X-ray diffraction (WAXS), Raman and attenuated total reflection Fourier transform infrared (ATR-FTIR) spectroscopies together with microscopy tools. Two significant properties of these composite films induced by light absorption were studied: a) the self-degradation of the films under sunlight and b) their self-cleaning or disinfection properties against Gram-negative (*Escherichia coli*) and Gram-positive (*Staphylococcus aureus*) bacteria upon UV excitation. The analysis of results provides evidence that, within the series of samples studied, the optimization of these two light-induced properties is related to specific morphological aspects of the oxide component. The different charge carrier species involved in the two processes allow rationalizing the self-degradation as a main function of primary particle size of the oxide component while the self-cleaning properties seem to be related to a more complex root on oxide morphological features, likely associated with particle–particle networking details.

## Introduction

Incorporation of titania in polymeric matrices emerges as a successful technology to fight against biological risks and guarantee the safety of products related to foods/beverages packaging or containers for biomedical/pharmaceutical materials/devices.[1] $TiO_2$-anatase is by far the most widely used photocatalyst, being a wide band-gap (3.0–3.2 eV) semiconductor that under UV illumination generates energy-rich electron-hole pairs able to degrade cell components of microorganisms without known weakness among bacteria, virus, fungi and/or protozoa.[1–3]

Here, EVOH–$TiO_2$ (EVOH, an ethylene–vinyl alcohol copolymer) composite films with potential use in the food packaging industry are considered.[4–8] Composite EVOH-based materials typically consist of a biocidal agent (carbonaceous phase, oxide or metal) to control growth of microorganisms[4–10] within an EVOH polymeric matrix. In this context and among potential inorganic fillers, $TiO_2$ offers unbeatable capabilities because, first of all, its biocidal action occurs without the need of releasing dangerous entities (on the contrary of silver, for example) and, additionally, because it allows degrading the polymer after its lifetime upon sunlight excitation, opening the gate of using a renewable energy source for an easy disposal of the polymer.[4] Moreover, the oxide typically enhances mechanical response of the final polymer based nanocomposites without significantly modifying the thermal ones.[1,4,11,12] Hence, $TiO_2$ appears as a multipurpose filler in polymer matrices with a number of important advantages concerning the improvement or maintenance of the physicochemical properties of the polymeric material as well as the addition of new capabilities including self-degradation and self-cleaning, opening a new deal of novel applications for the polymer matrix.

In the case of light-induced properties and particularly of the antimicrobial properties, we previously showed in the EVOH–$TiO_2$ system that the whole external composite surface can become biocidal by charge carrier transfer (specifically holes) from the anatase to the polymeric component.[4,6] This erases the need for anatase-microorganism contact and leads to non-contact, long-term and highly active biocidal materials. Among the paths to optimize biocidal properties of anatase, modification of this inorganic component by surface deposition using metals or oxides at low content has been mentioned.[13–22] The presence of limited amounts of Ag, Cu or Zn and other species at the anatase surface has been shown

[a]*Instituto de Catálisis y Petroleoquímica, CSIC, C/Marie Curie 2, 28049, Madrid, Spain. E-mail: mfg@icp.csic.es*
[b]*Instituto Ciencia y Tecnología de Polímeros, CSIC, C/Juan de la Cierva 3, Madrid, Spain. E-mail: martafg@ictp.csic.es*

to produce novel (*e.g.* non present in the corresponding, isolated *M*–$TiO_2$ and EVOH systems) effects on (UV/visible) optical properties without altering other physico-chemical features. However, an alternative path is to optimize the $TiO_2$ material itself without incorporation of additional (usually expensive ones, like silver) inorganic phases. While a number of contributions have been devoted to this topic using a significant number of different technologies,[1–11,23] we here focus on the use of simple modifications of the anatase phase in order to obtain improved light-induced self-cleaning and self-degradation properties.

Specifically, a first attempt typically pursues improvement of the optical excitation and de-excitation properties of the $TiO_2$ component by controlling the physico-chemical properties of the oxide.[1,24–26] While most of the previously mentioned works modified $TiO_2$ by surface/bulk doping, here we will concentrate on controlling light-triggered phenomena and, particularly, the charge handling after light excitation. In previous publications, we (and others) analyzed the synthesis and calcination of $TiO_2$ materials observing a direct link between calcination temperature of the materials, its morphological properties (particularly primary particle size), the defect distribution (particularly anion vacancies in the case of titania) and the final photocatalytic outcome.[2,3,27] We will try to study such effect using constant temperatures of calcination ranging from the minimum value where the anatase crystallization is complete (*ca.* 400–450 °C) to the maximum one that ensures the absence of rutile (600 °C). These two limits assure absence of amorphous or crystalline (other than anatase) phases and, additionally, the lack of impurities coming from incomplete elimination of residues from the synthesis (this being a typical impurity/dopant at surface that is not usually taken into account when discussing the optical properties of the solids). Note that impurity presence strongly alters charge carrier handling (trapping) after light excitation. Moreover, it can be stressed that the calcination step and the concomitant elimination of defects are critical points if highly active photoactive materials, exceeding the performance of typical reference ones as Evonik P25, have to be obtained.[2] The second effect concerns the inorganic–organic contact within the nanocomposite. The handling of the secondary particle size of the calcined oxide is the more straightforward way to improve the contact by decreasing its magnitude.[2] The use of sieving procedures appears as a simple, physical-like operation to control easily the secondary particle size.[28] As mentioned, optimum contact between the two components allows efficient charge separation upon light absorption and the use of holes at the whole nanocomposite surface.[4,13] Therefore, the efficiency of the EVOH–$TiO_2$ nanocomposite materials is expected to be directly related to the extent of the inorganic–organic interface.

In this contribution, we thus analyze four different EVOH–$TiO_2$ nanocomposite films where the morphological properties of the oxide as well as the inorganic–organic interface are modified in order to boost the light-triggered novel capabilities of the final materials. After their detailed multi-technique characterization and the measurement of their light-related novel properties, we will show that self-degradation and self-cleaning characteristics behave in different ways due to the fact that different charge carrier entities are involved in both processes. We will, however, prove that optimization of these two processes can be obtained in a single EVOH–$TiO_2$ material, providing thus the background for modern photoactive films with advanced properties.

## Experimental section

### Nanocomposite preparation

Bare $TiO_2$ (anatase) was prepared by using a microemulsion procedure.[27] Solid precursors attained from such method were used as obtained (samples numbered as one in their name) or sieved and subsequently selecting the portion with average aggregate size below 50 microns (samples labeled as two). After such treatments inorganic samples were calcined at 450 °C (samples A) or 600 °C (samples B) for a period of two hours in air. A summary of their main structural/morphological properties is given in Table 1. BET surface area of the bare $TiO_2$ materials was carried out by $N_2$ adsorption at 77 K using a Micromeritics 2010 instrument. XRD patterns of the pristine $TiO_2$ materials were recorded in the range $10^\circ < 2\theta < 120^\circ$ using 0.02° steps, using a Siemens D-501 diffractometer with Ni filter and graphite monochromator with a Cu $K_a$ X-ray source. The crystal size of anatase was determined from the most intense diffraction peak (101) using Scherrer equation.

A commercially available ethylene–vinyl alcohol copolymer (EVOH; Solvay), containing a nominal 71 mol% vinyl alcohol content, was used as polymeric matrix in the preparation of EVOH–$TiO_2$ nanocomposites at an inorganic content of 2 wt%. These novel materials were obtained by melt blending in a Haake Minilab twin screw extruder at 195 °C, a rotor speed of 100 rpm for 15 min. These processing conditions were optimized taking into account the final dispersion of nanoparticles and keeping away from EVOH degradation. Preceding this stage, nanoparticles and EVOH copolymer were previously sonicated (Sonics VC505) and stirred to achieve an initial homogeneous batch. After processing, specimens were manufactured as films of approximately 100 microns by compression molding in a Collin press between hot plates at 210 °C and at a pressure of 1.5 MPa for 5 min. A quench was applied to the different films from the melt to room temperature.

### Nanocomposites characterization

Transmission electron microscopy (TEM) was performed at room temperature in a 200 kV JEM-2100 JEOL microscope to analyze material homogeneity. Samples were cut in thin sections (40 nm) by cryoultramicrotomy (Leica EM UC6). Specimens were then deposited on copper grids. Scanning electron microscopy/energy dispersive X-ray spectroscopy (SEM/EDX) characterization of materials was carried out with Au–Pd (80 : 20) coated samples using an ESEM PHILLIPS equipment working at 25 keV. The WAXS patterns for the neat EVOH matrix and the distinct nanocomposites were recorded

 

**Table 1** Main physico-chemical characteristics of the $TiO_2$ components[a]

| Sample | Anatase crystal size (nm) | $S_{BET}$ ($m^2\ g^{-1}$) | Pore volume ($cm^3\ g^{-1}$) | Pore size (nm) |
|---|---|---|---|---|
| $TiO_2$-A1 | 9.7 | 94.7 | 0.098 | 3.4 |
| $TiO_2$-A2 | 10.0 | 84.6 | 0.084 | 3.3 |
| $TiO_2$-B1 | 17.0 | 31.7 | 0.081 | 7.1 |
| $TiO_2$-B2 | 17.3 | 26.1 | 0.063 | 6.0 |

[a] Anatase crystal size was determined using Scherrer equation. Standard deviation ($\pm$): 5% for crystal size, 1.5% for $S_{BET}$, 10% for the remaining observables. Total pore volume was taken at relative pressure $P/P_0 = 0.98$.

in the reflection mode at room temperature using a Bruker D8 Advance diffractometer equipped with a Goebel mirror and a PSD Vantec detector (from Bruker, Madison, Wisconsin). Cu-K$\alpha$ radiation was used and the equipment was calibrated with various standards. A step scanning mode was employed for the detector, with a $2\theta$ step of 0.024° and 0.2 s per step. The WAXS degree of crystallinity, $f_c^{WAXS}$, was determined from decomposition of X-ray patterns into crystalline diffractions and the amorphous halo with a fitting program. This amorphous peak was found to be centered at $2\theta$ of 19.9 $\pm$ 0.1° at the different samples. Raman spectra of the EVOH–$TiO_2$ nanocomposite films and the $TiO_2$ powders were collected with an inVia Raman microscope (Renishaw) equipped with a near-IR diode laser (785 nm) with a 1 $cm^{-1}$ spectral resolution.

The simulated photochemical degradation under sunlight was performed by using a Hamamatzu lamp L8868 with an intensity of 3500 mW $cm^{-2}$ (01 type at 365 nm). Changes were followed by Fourier transform infrared spectroscopy with an attenuated transmission reflection (ATR) cell mounted in a Perkin Elmer Spectrum One spectrometer (ATR-FTIR). The samples were situated at 6 cm of distance and considering an average daily sunlight intensity of *ca.* 2.72 mW $cm^{-2}$, the sample exposition during 20 h corresponds to about forty five days of sunlight exposition.

### Microbiological tests

The microorganisms used in this study include *Escherichia coli* 1337-H and *Staphylococcus aureus* 1341-H. They were obtained from the German Collection of Microorganisms and Cell Cultures (DSMZ, Braunschweig, Germany) and cultured and maintained according to the recommendations of the suppliers.[4,6] Briefly, *E. coli* 1337-H and *S. aureus* 1341-H were grown in Luria–Bertani (LB) medium at 37 °C using 100 mL flasks filled with 10 mL of the respective medium and subsequently used for photochemical cell viability assays. To study the antimicrobial activity of films, a suspension containing 10 μL of microbial cells (*ca.* $10^9$ CFU $mL^{-1}$) suspended in 1 mL broth solution was made.[29] Aliquots of 1 mL from these suspensions were added to a 4 mL quartz cubic cell containing 1 mL of sterilized water and the corresponding film under continuous stirring. The film-cell slurry was placed in the UV spectrometer chamber (Synergy HT Multi-Mode Microplate Reader, BioTek) and irradiated with a light at 280 nm (UV) for different time periods. The excitation line width is lower than 10 nm in all cases. As demonstrated by blank experiments, care was put into using a sub-lethal, maximum radiation energy fluence of *ca.* 1 kJ $m^{-2}$ throughout the study (60 min).

The four samples (A1, A2, B1 and B2 nanocomposite films) together with the reference (EVOH) were measured using the same bacterium inoculum for each microorganism tested. After irradiation and for different time intervals, aliquots of 100 μL were transferred to a 10 mL LB broth test tube. The order of cell dilution at this stage was $10^{-2}$. Loss of viability after each exposure time was determined by the viable count procedure on LB agar plates after serial dilution ($10^{-2}$ to $10^{-5}$). All plates were incubated at 37 °C for 24 h prior to enumeration after which they were scanned using a Bio-Rad Imaging System equipped with Analysis Software 4.6.5 (Bio-Rad) to enable enumeration of bacterial colonies among replicates. A minimum of four experimental runs was performed to determine antimicrobial activity; this leads to a standard error of $\pm$0.1 log CFU $mL^{-1}$ units in the reported results.

## Results and discussion

The $TiO_2$ component used in the study is, as can be seen in Table 1, relatively homogeneous, with rather scarce morphological modifications and always maintaining the anatase structure (see below). The rise of calcination temperature increases the particle size from *ca.* 10 to 17 nm while sieving leads to a more general modification of the morphological properties with a decrease ranging from *ca.* 10% (samples A*x*) to 20% (samples B*x*) in BET surface area and concomitant changes in pore size and volume. Although differences are, as said, relatively modest, B*x* samples are more strongly modified by the sieving procedure.

The interfacial contact between the $TiO_2$ nanoparticles and the EVOH polymer is illustrated in Fig. 1. This figure presents TEM views of the materials where dispersion of the oxide into the polymer matrix is shown. The numerical analysis of the inorganic aggregates is included in Table 2, screening more than 50 aggregates at each case. The Feret diameter was used to calculate the aggregate size distribution.[30] The size distribution first moment indicates a consistent decrease of the average aggregate size as a function of both, the increase of the calcination temperature as well as the sieving. Considering the primary particle size of the materials and assuming a similar ''packing'' density in all samples, these data mean that the number of primary oxides entities present in an aggregate is reduced by calcinations (from 450 to 600 °C) in *ca.* 80% while sieving decreases such number only by 13–15%. The

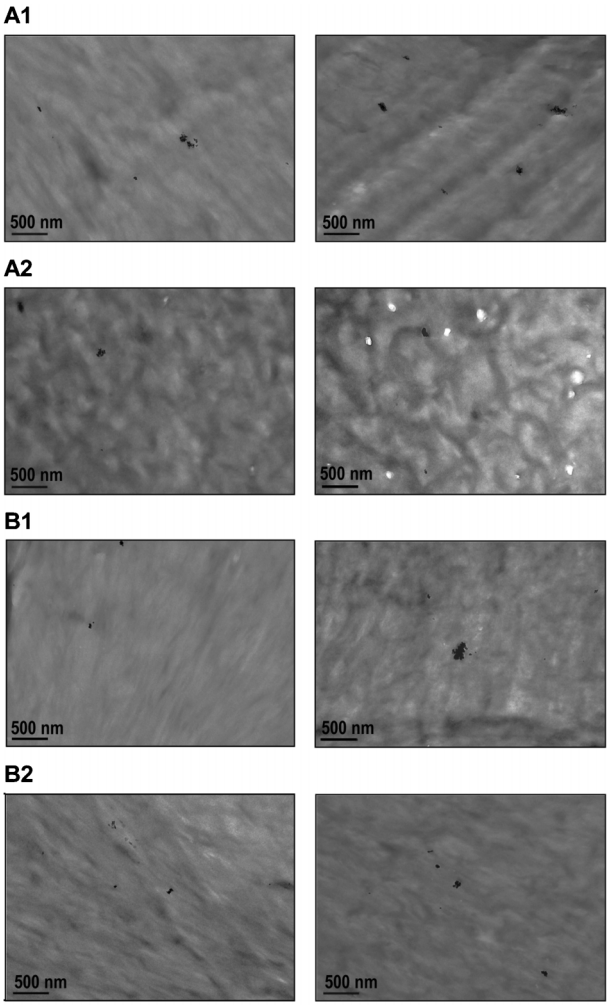


**Fig. 1** TEM images of A*x* and B*x* films.

third and four moment indicates relatively similar aggregate size distributions although A1 sample seems to present a larger tail (fourth moment) while samples B1 and B2 show greater third moment differences (but always positives; *e.g.* differences with respect to a normal distribution are more acute for aggregates with size above the mean). Series A*x* and

**Table 2** Characteristics of organic/inorganic crystalline phases for the different nanocomposites and for the EVOH polymer: $f_c^{WAXS}$ (crystallinity degree determined by WAXS at room temperature); also included the average aggregate size (first raw order moment), variance (second raw order moment) and higher normalized central moments of the anatase component size (Feret diameter) distribution[a]

| Sample | $f_c^{WAXS}$ | Size (nm) | Variance ($nm^2$) | Skewness (a.u.) | Kurtosis (a.u.) |
|---|---|---|---|---|---|
| A1 | 0.45 | 87.3 | 4371.5 | 0.76 | 4.0 |
| A2 | 0.45 | 74.0 | 3002.7 | 0.74 | 2.6 |
| B1 | 0.40 | 75.9 | 5446.1 | 0.97 | 2.4 |
| B2 | 0.45 | 66.4 | 1396.5 | 0.56 | 1.3 |

[a] Standard deviation (±) 7% for $f_c^{WAXS}$.

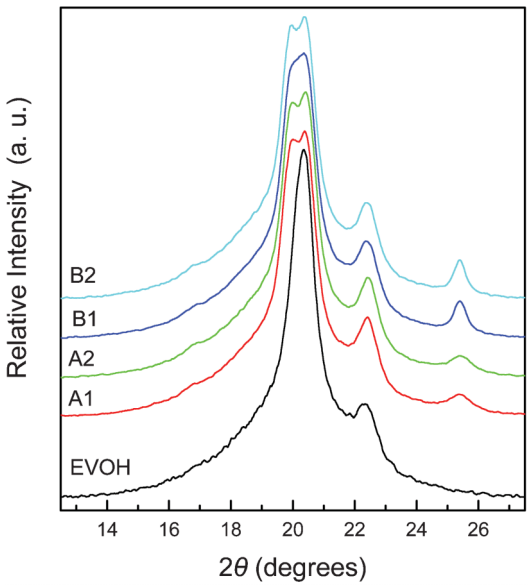


**Fig. 2** WAXS patterns at room temperature of the A*x* and B*x* samples and EVOH reference films.

B*x* undergo such changes displaying parallel trends. Overall, an increase of calcination temperature surprisingly leads to a decrease of the average aggregate particle size while sieving of the samples makes a similar (and, in this case, more predictable) decreasing trend. As described, other effects are visible in the aggregate size distribution but they are of more scarce nature. In any case, major differences appear to be present within the B*x* series as a function of the sieving. Hence as mentioned above, both series display a relatively similar behavior although some subtle differences associated with the particle size distribution, third and four moments, are more clearly observed in the B*x* series.

The structural properties of the materials prepared are analyzed using a combination of X-ray diffraction and Raman spectroscopy. Fig. 2 displays WAXS patterns of the samples. The EVOH copolymer is semicrystalline and, in addition, it exhibits polymorphism.[31–33] This polymorphism shown by EVOH copolymers is not the usual case concerning two unit cells with well-differentiated lattice parameters: in the present case, a continuous change of some of the lattice constants occurs by varying cooling rate during processing. For instance, the angle $\beta$ of the monoclinic lattice varies smoothly from an "equilibrium" value of about 92.2° in slowly crystallized (*i.e.* those cooled at 2 °C $min^{-1}$ from the melt) samples to a final value in quenched (cooling rate of around 80 °C $min^{-1}$) specimens of 90° (orthorhombic unit cell). The plot of the parent polymer (Fig. 2) is dominated by the 101 and 200 diffraction peaks characteristic of the EVOH orthorhombic cell.[31,32] The presence of $TiO_2$ is detected in the nanocomposite systems by appearance of the 101 reflection ascribed to the $TiO_2$ anatase polymorph (centered at *ca.* 25°; JCPDS-84-1286). No other titania phase (rutile) is visible. The anatase diffraction width changes with the primary particle size

 

differences of the oxide component in a fully consistent way from A*x* to B*x* series, as shown in Table 1. Anatase incorporation seems to promote a change of the EVOH crystalline lattice in the nanocomposites and, then, the profiles represent an intermediate state between the two modifications (*i.e.* orthorhombic to monoclinic cell). The crystallinity degree found in the different nanocomposites does not change much (see results reported in Table 2) except for the B1 that presents a value slightly lower. Thus, the diffraction study reveals relatively minor differences among the samples under study.

Raman spectroscopy was also used in order to determine the structural effects of anatase incorporation into the EVOH polymeric matrix. The frequency region dominated by EVOH peak contributions[34,35] is represented in Fig. 3a. Normalized intensities (considering the C–H stretching mode) confirm that local configuration of the polymer is relatively stable in the presence of $TiO_2$. To provide evidence of the $TiO_2$ stability in the incorporation process, an example of the Raman spectra in presence or absence of the polymer matrix is also shown (Fig. 3b). Anatase peaks at *ca.* 145, 395, 515 and 640 $cm^{-1}$ are discerned in the plot but here our attention will be focused on the lowest energy, larger intensity $E_g$ mode.[36] The analysis of this peak position shows minimal differences between the $TiO_2$ alone and within the nanocomposite (less than 1.5 $cm^{-1}$, therefore within experimental error), indicating again the absence of major changes during the preparation procedure.

A summary of the structural characterization of these EVOH–$TiO_2$ materials would thus point out that all samples display rather similar oxide aggregates although a trend of decreasing size and, then, of potentially increasing interactions with the polymer matrix is observed as the oxide calcination temperature is raised as well as sieving of the oxide precursor is applied. Such sieving makes rather similar effects on both series and only subtle differences were observed in the aggregate size distribution, concerning a minor tailing effect that appears more pronounced in the B*x* series. This general structural description of the $TiO_2$ status in the nanocomposite films would thus indicate that a characteristic improvement would be observed by increasing the calcination temperature as well as sieving of the inorganic precursor if light-triggered properties are exclusively driven by the extent of interface contact among phases. In the first case (calcination temperature) as mentioned in the introduction section, higher calcination temperature would also lead to a decrease in defects and, consequently, to a more optimum handling of charge carrier species, in turn favoring useful chemistry (for example, in this case, bacteria inactivation instead of charge recombination).[2]

Later on, the two more important light-induced new properties presented by the polymer-based films in presence of the oxide have been tested. Firstly, the self-degradation of the composite materials upon sunlight exposition was analyzed. Photo-degradability using a renewable energy source and, consequently, the production of environmentally friendly polymeric materials is a plus expected from $TiO_2$ addition to

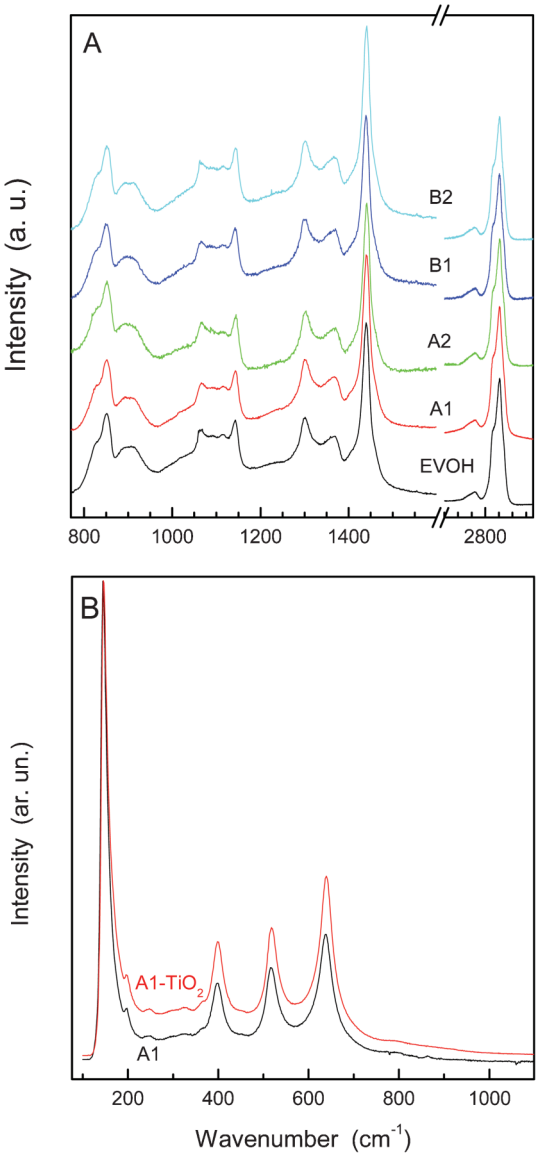


**Fig. 3** Raman spectra in the A) frequency region dominated by the EVOH polymer; B) frequency region of $TiO_2$ for the A1 sample (black spectrum) (polymer contribution has been subtracted for the sake of clarity) and the corresponding bare $TiO_2$ material (red spectrum).

the EVOH matrix. A simulated period of about one and a half months was studied. Fig. 4 displays selected ATR-FTIR spectra obtained during the process. While UV light is known to have a rather limited aging effect on EVOH polymers,[37] the progressive degradation of the polymeric matrix is evidenced in the case of the $TiO_2$-containing nanocomposites by the spectra displayed in the figure.

It is noticeable the apparent reduction in intensity and shift toward higher wavenumber (of *ca.* 60 $cm^{-1}$) of the broad band centered at around 3310 $cm^{-1}$. This latest trend is observed with increasing irradiation time, as clearly depicted in Fig. 5. This band is assigned to EVOH hydrogen bonded O–H stretching vibrations (negligible contribution of $TiO_2$ according to the average composition of the materials) and its

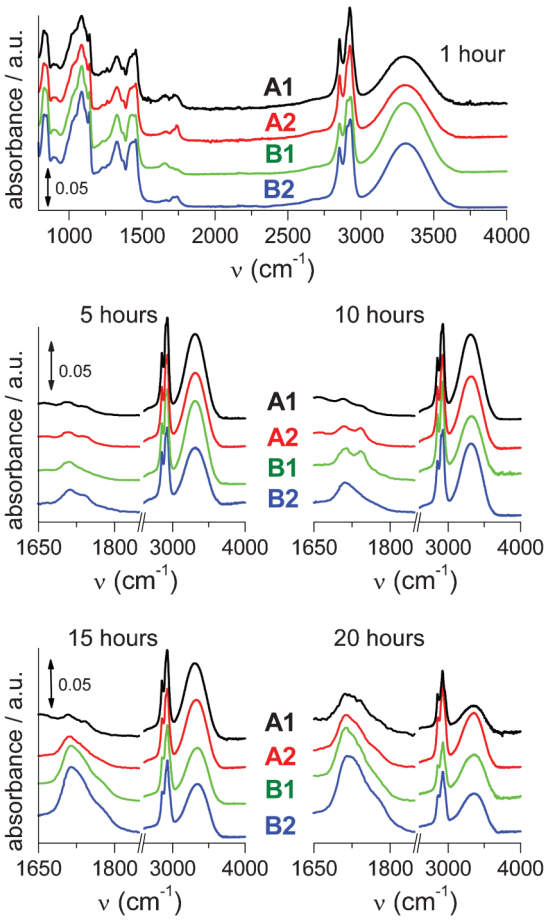


**Fig. 4** ATR-FTIR spectra of composite films subjected to sunlight aging for specific time treatments. Full spectra are presented at 1 h of treatment while selected regions are presented for other times.

broadness is thought to arise from a distribution of hydrogen bonded O–H groups of varying strength and geometry, coming from intra and intermolecular hydrogen bonded OH dimmer and multimers.[38] Some other changes that support transformation of these OH groups are noticed in the spectra (this range only shown in Fig. 4 for spectra taken at 1 h), at about 1330 and 1455 $cm^{-1}$, variations being associated with O–H deformation modes and showing a tendency to vanish as irradiation time is increased. Moreover, the vibration at around 1085 $cm^{-1}$ related to C–O stretching also appears to decrease. Nevertheless, a thorough analysis of the broad peaks in this "low frequency" spectroscopic range is complicated because of the large number of overlapped molecular vibrations. The shift of the band at 3310 $cm^{-1}$ to higher wavenumbers, represented in Fig. 5, is attributed to contributions of two different effects,[39] on one hand, the physical transformation of the hydroxyl groups vicinity and, on the other hand, the corresponding contribution originated from changes of dipolar and other intermolecular interactions. The overall variation suggests that there is a weakening of the inter- and intra-chain hydrogen-bonding interactions related, in one way or another, to the decrease of hydrogen-bonding elements with irradiation time because of their transformation.

The infrared spectra displayed in Fig. 4 show, simultaneously to all of the hydroxyl-related modifications, an obvious increase of intensity in the band appearing at around 1725–1710 $cm^{-1}$ as irradiation time rises. This band is attributed to presence of C=O stretching modes because of appearance of carbonyl groups[40,41] during UV irradiation. Such contribution is the most visible evidence of the oxidation process of the polymer matrix induced by sunlight.

In summary, all of these changes in the ATR-FTIR spectra provide evidence that the $TiO_2$ presence in the OH-rich hydrophilic zones of the EVOH polymer, where the degradation starts, leads to the formation of –CO moieties. The degradation by oxidation can be followed by the –CO peak/region intensity (Fig. 6) allowing establishing that the kinetics of the degradation process occurs in two main steps, with an initial, relatively slow period, followed by a faster, exponential-like behavior. Series B*x* appears to exhibit a quicker first

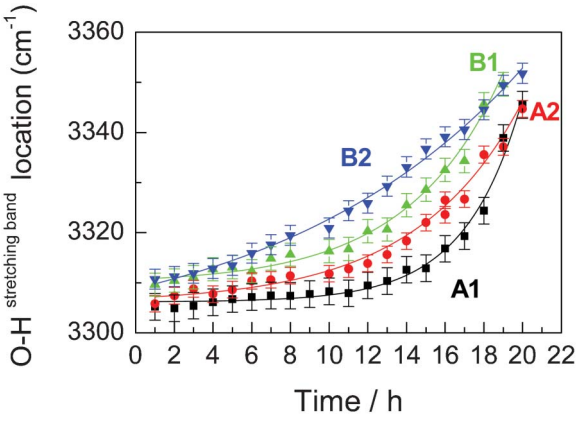


**Fig. 5** Frequency position of the OH region maximum (displayed in Fig. 4) as a function of sunlight treatment time.

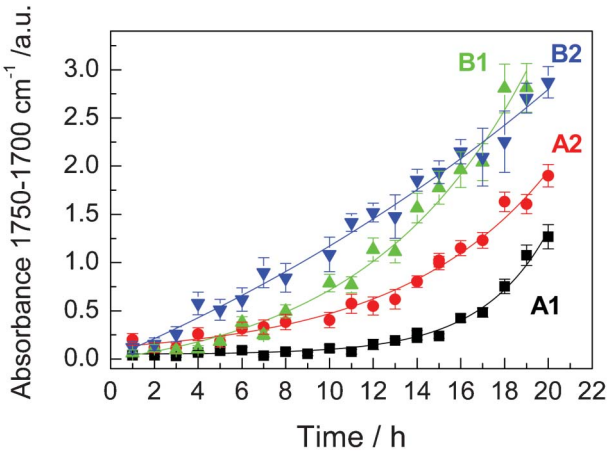


**Fig. 6** Intensity of the C=O stretch region displayed in Fig. 4 as a function of sunlight treatment time.

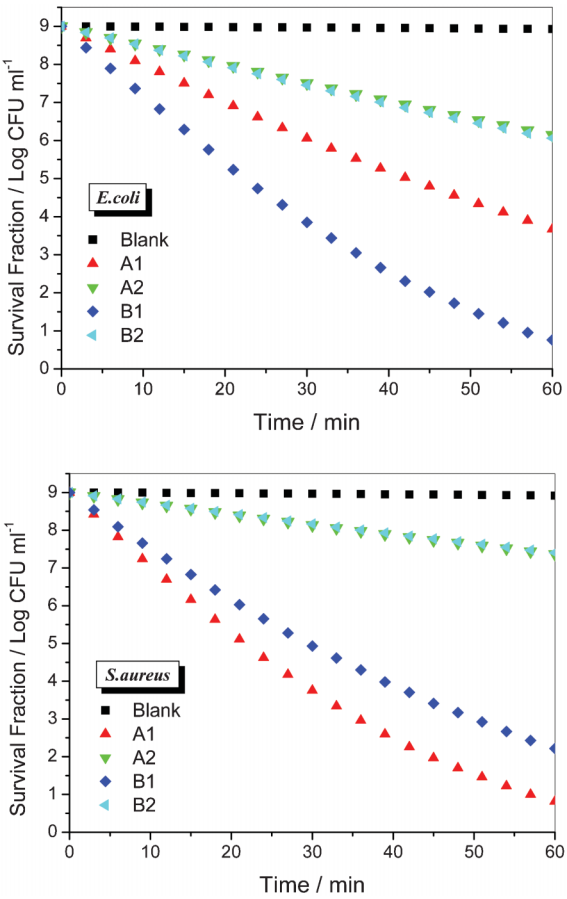


**Fig. 7** Process come-up logarithmic reduction of microorganism population suspended in LB medium. Survival curves of *E. coli* and *S. aureus* as function of irradiation time for EVOH/blank control and nanocomposite films.

period while series A*x* likely displayed a faster process for the second stage. Overall, the degradation degree of the polymer matrix observed by the end of the experiment is significantly larger in the B*x* series.

Fig. 7 displays the biocidal action of the materials for *E. coli* and *S. aureus* under UV light. Both Gram-negative (*E. coli*) and Gram-positive (*S. aureus*) bacteria have been tested in order to show the potential of these nanocomposites in the killing of microorganisms. The relatively innocuousness of the UV radiation is demonstrated by the blank experiments in presence of the EVOH matrix. This is due to the limited illumination fluences used in the experiments (see experimental section). The performance of the A1 samples has been previously analyzed with a total of 10 microorganisms including bacteria and yeasts, indicating the high biocidal potential of the nanocomposite even when comparing with other biocidal agents like silver, chemical compounds as hypochlorite and others.[4,6,13,17,20] It can be observed (Fig. 7) that the sample numbered 1 shows significantly superior activity with respect to sample named 2 in both series of films.

Comparison with previous results concerning efficiency of inorganic/organic biocidal agents is easy in the case of *E. coli*[42–49] and *S. aureus*.[50,51] There is also a significant number of works devoted to both pathogens.[1d,1i,52–61] Although antimicrobial tests are strongly dependent on the specific experimental conditions used, for a simple comparison we can indicate that our maximum log reduction of *ca.* 8.5/8.0, attained after 60 min upon UV light for, respectively, *E. coli*/*S. aureus*, could be compared, for example, with previous results on *E. coli* using polymer–$TiO_2$ nanocomposite films, with *ca.* 6.3, 4, 1, and 3 log-reduction for, respectively, 1,[54] 1,[61] 1,[55] and 0.3[1d] hour(s) of treatment. Moreover, it is interesting to stress that previous results using visible light for polymer–$TiO_2$ films gave relatively low (40%/1 h) deactivation performance against *E. coli*, far from that here presented.[49] Similarly, *ca.* 0.8, 1.0 and 3.0 log-reductions were reported after, respectively, 0.5,[54] 12[55] and 0.3[1d] hours of treatment in the case of *S. aureus*. As a summary, we can thus highlight the fact that A1/B1 samples appear highly biocidal while A2/B2 samples only render maximum values of the biokilling activity that are roughly half compared to the other (A1/B1) nanocomposite films. Even in the latter case, the final outcome is a competitive biocidal action, at least with respect to a significant number of previous works.[42–61] This fact can be attributed to the photo-chemical properties of the oxide component and, particularly, to an efficient charge handling after photo-excitation.

It is evident from results of Fig. 5 to 7 that the nanocomposite films perform quite differently in the two light-triggered properties analyzed. While the B*x* series seems to undergo a faster and deeper self-degradation process, the biocidal action seems superior for samples numbered 1 (A1/B1). Differences between the performance of the samples in the two light-induced processes, *e.g.* self-degradation and self-cleaning, can be rationalized by the fact that both are related to two different charge carrier species. While degradation (essentially an oxidation process) has been demonstrated to occur primarily by using electrons, the biocidal action is exclusively related to holes, the single species reaching the external film surface and responsible for the biokilling action.[4,6,17,18]

In anatase-titania, charge separation and handling after light absorption occurs through a multi-trapping process of electron while holes seem to have a faster decay as well as a faster travelling to the oxide surface.[2] Moreover, accumulation of trapped electrons at the bulk of the material is a well-known process that is, as mentioned, intimately connected with the number and nature of defects present.[2,3] As a primary rule, it can be noted that the number of defects is inversely proportional to the primary particle size of the oxide component and would thus give a rationalization for the faster and deeper degradation of the B*x* nanocomposite films with respect to A*x* ones. Electrons, responsible for the production of CO moieties in presence of oxygen, are thus driving the oxidation process of the polymer matrix with differences among nanocomposites systems related exclusively to the primary particle size of the oxide component.

Holes availability at the external surface of the nanocomposite films seems, on the other hand, to be larger for A1/B1 samples, despite the fact that the aggregate particle size of the

oxide component displays the two larger values in these two films (Table 2). As the contact with the polymer seems to be carried out in all cases with the same polymer region (hydrophilic, non-crystalline part of the polymer, which according to Raman is essentially equal in all samples) and the A*x*, B*x* samples present a constant inorganic primary particle size within the corresponding series (Table 1), we can suggest that a different hole charge handling occurs as a function of the morphological properties of the inorganic phase. The morphology of the oxide components (Table 1, pore volume and size) seems to vary in a larger degree in the B*x* series than the A*x* ones but no clear trend can be spotted to justify the results. Although a definitive answer cannot be given here, it can be nevertheless suggested that details of the oxide particle–particle contact are critical to allow the adequate charge separation and subsequent holes transfer to the oxide–polymer interface. Of course, such morphological details cannot be easily studied even with the help of high resolution microscopy, which would demand an extensive study of the oxide and composite films.

To summarize, it can be mentioned that although the inorganic–organic interface contact plays a key role to allow charge transfer within the nanocomposite components after light excitation,[1,4,6,13,16] in our samples, where the components contact is relatively similar, important performance differences nevertheless appear in self-degradation and self-cleaning properties. Such differences can be rationalized as a function of the oxide morphological properties as above discussed. The combined analysis of the self-cleaning and self-degradation properties indicates that the A1 samples may be the optimum choice for obtaining novel, dual-action food packaging films as it controls the damage of the polymer to a reasonable extent in a period of *ca.* one and a half months and has an outstanding biocidal capability against both Gram-negative and Gram-positive bacteria. It can be particularly mentioned that the self-degradation of the polymer is rather slow for the initial period of about one month of continuous sunlight exposure, further demonstrating the suitability of the system for the mentioned application. The B1 sample is also highly biocidal but renders both a faster and more extended damage of the polymeric matrix. So, the present study provides two highly biocidal samples with adjustable effect on the polymeric matrix as a function of the lifetime required.

## Conclusions

In this report, the effect of $TiO_2$ morphology on the performance of EVOH–$TiO_2$ nanocomposite films under light for producing self-sterilized and self-degradation materials is investigated. From a single preparation of the inorganic component, four different titania samples are obtained by sieving (or not) and calcination at two different temperatures. Anatase materials are observed in all cases with primary particle size ranging from 9.7 to 17.3 nm.

The inclusion of the four $TiO_2$ fillers in the EVOH matrix yields four nanocomposite materials with relatively similar structural characteristics. All samples display similar oxide aggregates, below 100 nm, although a trend to lower size and, thus, to potentially (moderately) promoting larger interaction with the polymer matrix is observed while increasing the oxide calcination temperature as well as by sieving the oxide precursor. Such sieving makes, to a first approximation, similar effects on both series and only subtle differences are observed in the aggregate size distribution concerning a minor tailing effect that appears more pronounced in the B*x* series. Due to the fact that the oxide phase does not show large differences within nanocomposite samples and that the polymeric component is similarly affected by the oxide inclusion in all materials, the inorganic–organic interface is expected to display rather analogous properties in all the samples studied and its surface would be proportional to the average aggregate particle size of the nanocomposite films. Of note, strong performance differences are nevertheless observed in the light-induced self-cleaning and self-degradation properties of the nanocomposite films here studied without apparent correlation with the inorganic–organic interface extent. Instead, both (differential among our samples) properties are mostly rationalized in terms of the specific morphological properties of the oxide component dispersed into the polymeric matrix. An optimum performance, concerning minimum degradation of the polymeric matrix and high biocidal activity, is achieved with the A1 composite film. Such nanocomposite material appears thus as a striking, dual-action material with high light-triggered capabilities.

## Acknowledgements

Financial support (CTQ2010-14872/BQU, PLE2009-0037, PRI-PIBJP-2011-0914, MAT2010-17016, MAT2010-19883) is fully acknowledged. The research leading to some of these results has also received funding from the European Union's Seventh Framework Programme (FP7/2007-2013) under grant agreement no. 253445. K.C.C. and A.K. thank, respectively the Marie Curie (FP7-PEOPLE-2009-IEF-253445) and MINECO program ''Ramón y Cajal'' for postdoctoral fellowships.

## Notes and references

1 (*a*) O. Carp, C. L. Huisman and A. Reller, *Prog. Solid State Chem.*, 2004, **32**, 33; (*b*) O. K. Dalrymple, E. Stefanakos, M. A. Trozt and D. Y. Goswany, *Appl. Catal., B*, 2010, **98**, 27; (*c*) C. P. Dunlop, S. Sheeran, J. A. Bryne, M. A. S. McMahon, M. A. Boyle and K. G. McGuigan, *J. Photochem. Photobiol., A*, 2010, **216**, 303; (*d*) H. Kong, J. Song and J. Jang, *Environ. Sci. Technol.*, 2010, **44**, 5672; (*e*) T. V. Duncan, *J. Colloid Interface Sci.*, 2011, **363**, 1; (*f*) H. A. Foster, I. B. Ditta, S. Varghese and A. Steele, *Appl. Microbiol. Biotechnol.*, 2011, **90**, 1847; (*g*) J. Luan, S. Wong, Z. Hu and L. Zhang, *Curr. Org. Synth.*, 2012, **9**, 114; (*h*) A. Llorens, E. Lloret, P.

 

A. Picouet, R. Trbjevich and A. Fernández, *Trends Food Sci. Technol.*, 2012, **24**, 19; (*i*) W. Bahloul, F. Mélis, V. Bounor-Legeré and P. Cassagnau, *Mater. Chem. Phys.*, 2012, **134**, 399; (*j*) A. Muñoz-Bonilla and M. Fernández-García, *Prog. Polym. Sci.*, 2012, **37**, 281; (*k*) H. Bodaghi, Y. Mostofi, A. Oromiehie, Z. Zamani, B. Ghanbarzadeh, C. Costa, A. Conte and M. A. Del Nobile, *LWT–Food Sci. Technol.*, 2013, **50**, 702.

2 A. Kubacka, M. Fernández-García and G. Colón, *Chem. Rev.*, 2012, **112**, 1555.

3 X. Chen and S. S. Mao, *Chem. Rev.*, 2007, **107**, 2891.

4 A. Kubacka, C. Serrano, M. Ferrer, H. Lünsdorf, P. Bielecki, M. L. Cerrada, M. Fernández-García and M. Fernández-García, *Nano Lett.*, 2007, **7**, 2529.

5 Y. Wang, M. Zhong, F. Chen and J. Yang, *Appl. Catal., B*, 2009, **90**, 249.

6 M. L. Cerrada, C. Serrano, M. Sánchez-Chaves, F. Fernández-Martín, A. de Andrés, R. Jiménez-Riobóo, M. Fernández-García, A. Kubacka, M. Ferrer and M. Fernández-García, *Adv. Funct. Mater.*, 2008, **18**, 1949.

7 A. Peter, C. Nicula, A. Mihaly-Cozmula, L. Mihaly-Cozmula and E. Indea, *Int. J. Food Sci. Technol.*, 2012, **47**, 1448.

8 P. A. Sreekumar, M. A. Al-Harthi and S. K. De, *J. Compos. Mater.*, 2012, **46**, 3181.

9 A. Martínez-Abad, J. M. Lagarón and M. J. Ocio, *J. Agric. Food Chem.*, 2012, **60**, 5350.

10 P. Lei, F. Wang, X. Gao, Y. Din, S. Zhang, J. Zhao, S. Liu and M. Yang, *J. Hazard. Mater.*, 2012, **227–228**, 185.

11 Y. Zhu, G. C. Buonocore, M. Larirgne and L. Ambrosio, *Polym. Compos.*, 2011, **32**, 519.

12 A. Kubacka, M. Ferrer, M. L. Cerrada, C. Serrano, M. Sánchez-Chaves, M. Fernández-García, A. de Andrés, R. J. Jiménez-Riobóo, F. Fernández-Martín and M. Fernández-García, *Appl. Catal., B*, 2009, **89**, 441.

13 A. Kubacka, C. Serrano, M. L. Cerrada, M. Fernández-García, M. Ferrer and M. Fernández-García, *J. Phys. Chem. C*, 2009, **113**, 9182.

14 A. Emamifar, M. Kadivar, M. Shahedi and S. Soleimanian-Zad, *Food Control*, 2010, **22**, 408.

15 D. Wodka, E. Bielaniska, R. P. Socha, M. Elzbieciak-Wodka, J. Gurgul, P. Nowak, P. Warszynxki and I. Kumariki, *ACS Appl. Mater. Interfaces*, 2010, **9**, 1945.

16 S. H. Hwang, J. Song, Y. Jung, O. Y. Kweon, H. Song and J. H. Jang, *Chem. Commun.*, 2011, **47**, 9164.

17 T.-T. Tsai, W.-P. Sung and W. Song, *Environ. Sci. Technol.*, 2011, **28**, 635.

18 A. Kubacka, M. Ferrer, M. L. Cerrada, C. Serrano, M. Fernández-García and M. Fernández-García, *Appl. Catal. B*, 2011, **89**, 441.

19 C. Karunakaran, G. Abiramasundari, P. Gomathisankar, G. Manikandan and V. Anandi, *Mater. Res. Bull.*, 2011, **46**, 1586.

20 A. Kubacka, M. Ferrer and M. Fernández-García, *Appl. Catal. B*, 2012, **121–122**, 230.

21 L. Liu, Z. Liu, H. Bai and D. D. Sun, *Water Res.*, 2012, **46**, 112.

22 X.-D. Zhou, F. Chen, J.-T. Yang, X.-H. Yan and M.-Q. Zhong, *Mater. Sci. Eng., C*, 2013, **33**, 1209.

23 M. Sokmen, T. Tatlidil, C. Breen, F. Clegg, C. K. Buruk, T. Sivlim and S. Akkan, *J. Hazard. Mater.*, 2011, **187**, 199.

24 J. Li and J. Z. Zhang, *Coord. Chem. Rev.*, 2009, **253**, 3015.

25 S. Sontakke, J. Modrak and G. Madras, *Chem. Eng. J.*, 2010, **165**, 225.

26 S. Sontakke, C. Mohan, J. Modrak and G. Madras, *Chem. Eng. J.*, 2012, **189–190**, 101.

27 M. Fernández-García, C. Belver, J. C. Hanson, X. Wang and J. A. Rodriguez, *J. Am. Chem. Soc.*, 2007, **129**, 13604.

28 J. Araña, J. M. Doña-Rodríguez, D. Portillo-Carrizo, C. Fernández-Rodríguez, J. Pérez-Peña, O. González-Díaz, J. A. Navío and M. Macías, *Appl. Catal., B*, 2010, **100**, 346.

29 M. Ferrer, J. Soliveri, F. J. Plou, N. López-Cortés, D. Reyes-Duarte, M. Christensen, J. L. Copa-Patiño and A. Ballesteros, *Enzyme Microb. Technol.*, 2005, **36**, 391.

30 R. J. Matyi, L. H. Schartz and J. B. Butt, *Catal. Rev. Sci. Eng.*, 1987, **29**, 41.

31 K. Nakamae, M. Kameyama and T. Matsumoto, *Polym. Eng. Sci.*, 1979, **19**, 572.

32 M. L. Cerrada, E. Pérez, J. M. Pereña and R. Benavente, *Macromolecules*, 1998, **31**, 2559.

33 M. L. Cerrada, F. Fauth, J. P. Fernández-Blázquez and E. Pérez, *Polym. Int.*, 2010, **59**, 1141.

34 R. J. González, R. Zallen and H. Berger, *Phys. Rev. B: Condens. Matter*, 1997, **55**, 7014.

35 B. Erlandsson, S. Karlsson and A.-C. Albertsson, *Acta Polym.*, 1998, **49**, 363.

36 S. Kelly, F. H. Pollak and M. Tomkiewicz, *J. Phys. Chem. B*, 1997, **101**, 2730.

37 D. J. Carlsson, S. Chmela and D. M. Wiles, *Polym. Degrad. Stab.*, 1991, **31**, 255.

38 M. M. Coleman, X. Yang, H. Zhang and P. C. Painter, *J. Macromol. Sci., Part B: Phys.*, 1993, **32**, 295.

39 D. J. Skrovanek, S. E. Howe, P. C. Painter and M. M. Coleman, *Macromolecules*, 1985, **18**, 1676.

40 Z. Su, Y. Zhao, X. Zhang, S. Zhu, D. Wang, J. Wu, C. C. Han and D. Xu, *Macromolecules*, 2004, **37**, 3249.

41 E. Folder and B. Pokanzky, *J. Colloid Interface Sci.*, 2005, **283**, 79.

42 Z. Huang, P. C. Maness, D. M. Blake, E. J. Wolfrum, S. L. Smolinski and W. A. Jacoby, *J. Photochem. Photobiol., A*, 2000, **130**, 163.

43 J. A. Ibañez, M. I. Litter and R. A. Pizarro, *J. Photochem. Photobiol., A*, 2003, **157**, 81.

44 J. M. C. Robertson, P. K. Robertson and L. A. Lawton, *J. Photochem. Photobiol., A*, 2003, **157**, 51.

45 M. Cho, H. Chung, W. Choi and J. Yoon, *Water Res.*, 2004, **38**, 1069.

46 J. Joo, S. G. Kwon, T. Yu, M. Cho, J. Lee, J. Yoon and T. Hyeon, *J. Phys. Chem. B*, 2005, **109**, 15297.

47 J. Lonnen, S. Kilvington, F. Al-Touati and K. G. McGuigan, *Water Res.*, 2005, **39**, 877.

48 K.-Y. You, J. H. Byeon, J.-H. Park and J. Hwang, *Sci. Total Environ.*, 2007, **373**, 572.

49 X. Zhang, H. Su, Y. Zhao and T. Tau, *J. Photochem. Photobiol., A*, 2008, **199**, 123.

50 C. Ho, J. Tobis, C. Sprich, R. Thomann and J. C. Tiller, *Adv. Mater.*, 2004, **16**, 957.

51 J. W. Arnol, D. H. Boothe and B. W. Mitatell, *J. Appl. Poult. Res.*, 2004, **13**, 200.

52 O. Seven, B. Dinder, S. Aydemir, D. Metin, M. A. Ozinel and S. Icli, *J. Photochem. Photobiol., A*, 2004, **165**, 103.

53 D. Mitoraj, A. Janczyk, M. Strus, H. Kirsh, G. Stochel, P. B. Heczko and W. Macyk, *Photochem. Photobiol. Sci.*, 2007, **6**, 642.
54 K. P. Kuhn, I. F. Chaberny, K. Massholder, M. Stickler, V. W. Benz, H.-G. Sonnatg and L. Erdinger, *Chemosphere*, 2003, **53**, 71.
55 Z. Wang, G. Li, H. Peng, Z. Zhang and X. Wang, *J. Mater. Sci.*, 2005, **40**, 6433.
56 K. Page, R. G. Palgrave, P. Parkin, M. Wilson, S. L. P. Sarin and A. V. Chadwick, *J. Mater. Sci.*, 2007, **17**, 95.
57 A. Vohra, D. Y. Goswami, D. A. Deshpande and S. S. Block, *Appl. Catal. B*, 2006, **65**, 57.
58 M. M. Cowan, K. Z. Abshire, S. L. Houk and S. M. Evans, *J. Ind. Microbiol. Biotechnol.*, 2003, **30**, 102.
59 A. Oyama, Y. Yokoyama, M. Uchida and A. Ito, *Biomaterials*, 2006, **27**, 3295.
60 Q. Zhang, C. Sun, Y. Zhao, S. Zhou, X. Hu and P. Chen, *Environ. Sci. Technol.*, 2010, **44**, 3270.
61 P. A. Zapata, H. Palza, K. Delgado and F. M. Rabagliati, *J. Polym. Sci., Part A: Polym. Chem.*, 2012, **50**, 4055.

 